Chemistry–A European Journal
Research Article
doi.org/10.1002/chem.202202318
Chemistry Europe
European Chemical Societies Publishing
www.chemeurj.org

Room-Temperature Solid-State Transformation of $Na_4SnS_4 \cdot 14H_2O$ into $Na_4Sn_2S_6 \cdot 5H_2O$: An Unusual Epitaxial Reaction Including Bond Formation, Mass Transport, and Ionic Conductivity

Assma Benkada,[a] Felix Hartmann,*[a] Tobias A. Engesser,[a] Sylvio Indris,[b] Tatiana Zinkevich,[b] Christian Näther,[a] Henning Lühmann,[a] Helge Reinsch,[a] Stefan Adams,[c] and Wolfgang Bensch*[a]

Abstract: A highly unusual solid-state epitaxy-induced phase transformation of $Na_4SnS_4 \cdot 14H_2O$ (**I**) into $Na_4Sn_2S_6 \cdot 5H_2O$ (**II**) occurs at room temperature. Ab initio molecular dynamics (AIMD) simulations indicate an internal acid-base reaction to form $[SnS_3SH]^{3-}$ which condensates to $[Sn_2S_6]^{4-}$. The reaction involves a complex sequence of O–H bond cleavage, S^{2-} protonation, Sn–S bond formation and diffusion of various species while preserving the crystal morphology. In situ Raman and IR spectroscopy evidence the formation of $[Sn_2S_6]^{4-}$. DFT calculations allowed assignment of all bands appearing during the transformation. X-ray diffraction and in situ ^{1}H NMR demonstrate a transformation within several days and yield a reaction turnover of ≈0.38 %/h. AIMD and experimental ionic conductivity data closely follow a Vogel-Fulcher-Tammann type T dependence with $D(Na) = 6 \times 10^{-14}$ m^2 s^{-1} at $T = 300$ K with values increasing by three orders of magnitude from −20 to +25 °C.

Introduction

Over the last few decades, a large variety of synthetic approaches have been developed for the synthesis of thiostannates or tin sulfides. These include the molten flux approach,[1,2] conventional high temperature reactions,[3–5] solvothermal methods,[6–9] or reactions in liquid media at moderate temperatures.[10,11] Beside the most common thiostannate anion, $[Sn_2S_6]^{4-}$, which is composed of two edge-sharing $[SnS_4]$ tetrahedra, a range of further $[Sn_nS_{2n+x/2}]^{x-}$ units like $[SnS_4]^{4-}$, $[Sn_3S_7]^{2-}$ or $[Sn_4S_9]^{2-}$ are also observed with Sn^{IV} valence.[6] In addition, many examples have been reported for compounds with mixed Sn valence, such as Sn^{IV}/Sn^{II} or Sn^{IV}/Sn^{III}.[12–14] The structural versatility is due to the variable coordination number (CN = 4–6) as well as the variable oxidation state of Sn. We recently identified $Na_4SnS_4 \cdot 14H_2O$ (**I**)[15] as a promising starting material for the preparation of new thiostannates from liquid media.[10,11] These syntheses yield rather complex anionic species instead of the simple SnS_4^{4-} anion.[10,11] We evidenced that **I** spontaneously undergoes an acid-base reaction in H_2O and $[Sn_2S_6]^{4-}$ is formed under release of H_2S.[11] In addition, we successfully used **I** and mixtures with $Na_3SbS_4 \cdot 9H_2O$ for the generation of a new Na_4SnS_4 polymorph and Na^+ superionic conductors $Na_{4-x}Sn_{1-x}Sb_xS_4$ by directed thermal removal of the crystal water molecules at a moderate temperature.[16] This powerful and economic synthetic route appears promising for transfer into industrial application provided that certain prerequisites are fulfilled. In particular, the process-relevant properties of the starting compounds must be known, and suitable candidates should be i) easy to synthesize including scalability, reproducibility and high purity; ii) composed of cheap, earth-abundant, non-toxic and sustainable elements; iii) long-term stable under ambient conditions.

Compound **I** contains a large amount of crystal water molecules and such compounds tend to decompose slowly. Therefore, we here studied the stability and reactivity of **I** and surprisingly, we found a slow epitaxial reaction transforming **I** into $Na_4Sn_2S_6 \cdot 5H_2O$ (**II**) at room temperature (RT). In this study, we monitored this unusual structural transformation in the solid state with ex situ X-ray powder diffraction (XRPD), in situ

[a] Dr. A. Benkada, F. Hartmann, Dr. T. A. Engesser, Prof. Dr. C. Näther, H. Lühmann, Dr. H. Reinsch, Prof. Dr. W. Bensch
Institute of Inorganic Chemistry
Christian-Albrecht University of Kiel
Max-Eyth-Str. 2, 24118 Kiel (Germany)
E-mail: fhartmann@ac.uni-kiel.de
wbensch@ac.uni-kiel.de
[b] Dr. S. Indris, Dr. T. Zinkevich
Institute for Applied Materials – Energy Storage Systems
Karlsruhe Institute of Technology
P.O. Box 3640, 76021 Karlsruhe (Germany)
[c] Prof. Dr. S. Adams
Department of Materials Science and Engineering
National University of Singapore
Singapore 117579 (Singapore)

Supporting information for this article is available on the WWW under https://doi.org/10.1002/chem.202202318

Raman, in situ IR, and in situ NMR spectroscopy. The multi-method experimental characterization of this unusual structural transformation is complemented by an investigation of the underlying dynamics with the help of ab initio molecular dynamics (AIMD) simulations and an analysis of the consequences of the transformation on the Na^+ ion conductivity in both phases.

Results and Discussion

The storage atmosphere plays a crucial role for preserving the integrity of **I**: at 95% relative humidity (RH) complete degradation occurs to form a mushy solid within 3 d; at RH = 59% small amounts of $Na_4Sn_2S_6 \cdot 5H_2O$ (**II**) were formed after 1 d (Figure S1). Storing the sample in vacuum, Ar or covered by Scotch tape also resulted in a partial transformation (Figure S1). This transformation process was investigated in ambient air (RH: 35-40%) collecting XRPD patterns at regular intervals (Figure 1). The initial XRPD pattern demonstrates phase purity of **I**, reflections of **II** appeared after 1 d and the amount of **II** steadily increased but even after 11 d no full transformation was achieved. A two-phase Rietveld refinement showed that ≈15 wt% of **I** was transformed into **II** after 11 d. But one should consider this value with some care because a pronounced preferred orientation in the pattern of **I** caused by the platelet-like crystals rather yields an estimate than an exact value.

The full width at half maximum (FWHM) of the reflections does not differ significantly between **I** and **II**, most probably pointing at an intra-crystalline process. Hence, we propose that this structural transformation is thermodynamically driven with **I** being less stable at RT than **II** under the storage conditions. This is supported by the observation, that no transformation occurs for months storing **I** in a freezer ($T = -18\,°C$).

Obviously, a condensation reaction occurs in the solid state involving i) protonation of $[SnS_4]^{4-}$ at S^{2-} by proton transfer from H_2O, i.e. an O–H bond breakage occurs, ii) condensation of adjacent $[SnS_3SH]^{3-}$ anions to generate $[Sn_2S_6]^{4-}$, and iii) H_2S release as verified using humid Pb acetate paper. These processes are thermally activated including mass transport and diffusion of species in the crystal with a reasonably high ion mobility. For retaining mass balance, amorphous NaOH must be generated according to the chemical Equation (1):

$$2\ Na_4SnS_4 \cdot 14H_2O \rightarrow Na_4Sn_2S_6 \cdot 5H_2O + 19\ H_2O + 2\ H_2S + 4\ NaOH \quad (1)$$

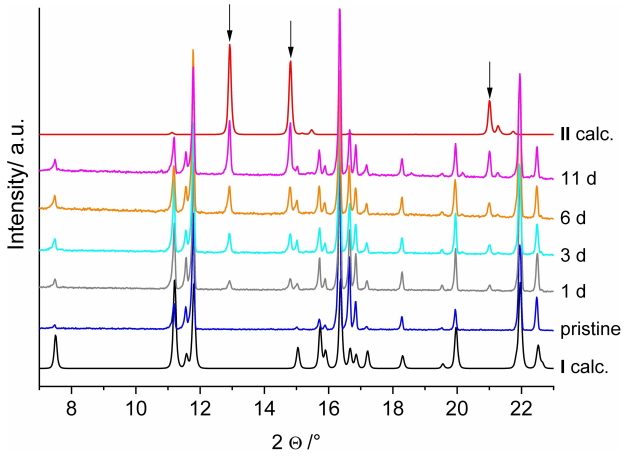

Figure 1. XRPD patterns of **I** recorded at different time intervals in air. Arrows are drawn for highlighting the development of reflections of **II**.

The structural transformation is accompanied by a significant density increase from 1.856 to 2.445 g/cm^3 and is initiated at various nucleation spots in crystals of **I** as observed by optical microscopy (Figure S2).

Comparing the unit cell parameters of **I** and **II** some surprising similarities are identified: the lattice parameters for **I** are $a = 8.62311(15)$, $b = 23.5067(3)$, $c = 11.3086(2)$ Å and $\beta = 110.4827(19)°$, while those of **II** are $a = 8.45088(3)$ and $c = 23.32912(12)$ Å, i.e. the *a*- and *b*-axes of **I** match well with *a*- and *c*-axes of **II** indicating an epitaxial relation between the structures (Figure 2). The monoclinic space groups (SG) *C*2/*c* with disorder of one Na atom and five H atoms[15] and *Cc*[17] were reported for **I**. A redetermination of the structure by single-crystal X-ray diffraction (SC-XRD) shows that SG *C*2/*c* is correct (further details in Supporting Information). Structure determination of **I** at various temperatures (Table S1) reveals a linear unit cell expansion (Figure S4) with increasing temperature and almost isotropic atomic displacement parameters for Na^+ ions (Figure S5).

In the structure of **I**, Na1 is octahedrally coordinated by five H_2O molecules and one S^{2-} anion, while Na2/Na3 are in an octahedral environment of six H_2O molecules (Figure 2, top and Figure S6). All bond lengths are in the range of the sum of ionic radii [r_{Na} (CN = 6): 1.02 Å, O^{2-}: 1.35 Å, S^{2-}: 1.84 Å; Sn^{4+}: 0.55 Å; Table S2][18] and match literature data.[2,5, 19, 20] The plausibility of the structure model is also underlined by the global instability index GII, i.e. the root mean squared average bond valence sum mismatch, which is 0.17 and hence in the acceptable range < 0.2 both for *C*2/*c* as for *Cc*. The Na^+ centered polyhedra are connected through common corners and edges to form a 3D structure (Figure 2, top). Only one of the two unique S^{2-} anions of $[SnS_4]^{4-}$ has bonds to Na^+ ions. A special structural feature is the connection of two $[SnS_4]^{4-}$ anions by unsymmetrical S···H–O bonds with one remarkable short S···H bond of 2.36 Å and one longer at 2.57 Å (O–H···S angles: 170 and 157°), indicating strong hydrogen bonds (Figure 2, top). This geometric situation may allow protonation of the terminal atoms of the $[SnS_4]^{4-}$ anions. Only five H_2O molecules are involved in O–H···O bonding, but all in O–H···S bonds (Table S3).

Compound **II**, $Na_4Sn_2S_6 \cdot 5H_2O$, (SG: $P4_12_12$) comprises Sn, Na1, Na2, S2, S4, O2 and O3 atoms in general and S1, S3 and O1 in special positions (Figure S7 and Table S4). In the $[Sn_2S_6]^{4-}$ anion the Sn-S_{brid} bond is longer compared to the Sn-S_{term} bonds (Table S5),[21] and the angles around Sn indicate a small distortion of the tetrahedra, in agreement with literature.[22–28] All S^{2-} anions of $[Sn_2S_6]^{4-}$ have bonds to Na^+: S_{brid} (S1, S3) have bonds to two Na^+ and S_{term} (S2, S4) are involved in one respectively three Na–S bonds (Figure 2, bottom). While the

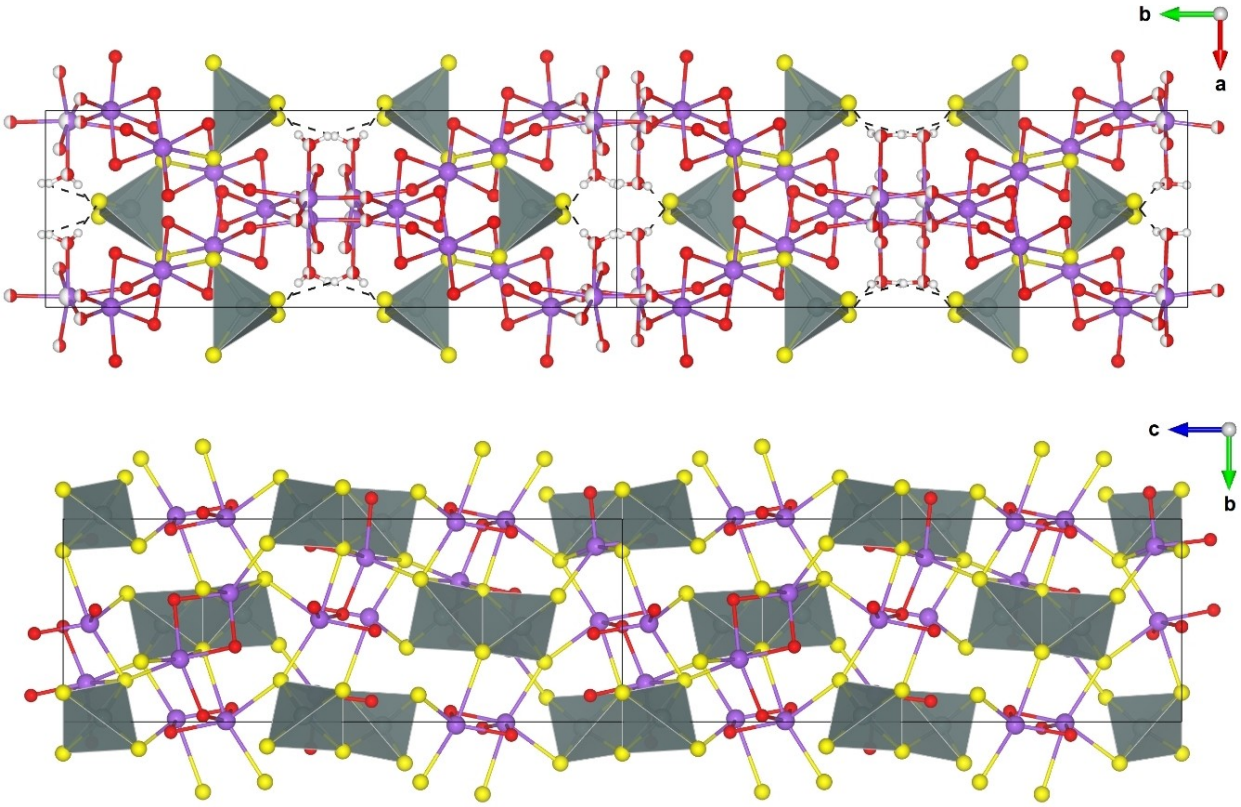

Figure 2. View of the interconnection of different polyhedra in the structures of **I** (top) and **II** (bottom). Two-unit cells along [010] (**I**) containing the split positions O5, O6 and O7 (left) and O5′, O6′ and O7′ (right) and along [001] (**II**) are displayed. Only $[SnS_4]^{4-}$ and $[Sn_2S_6]^{4-}$ units are drawn as polyhedra. Only H atoms involved in special S···H–O interactions (dashed lines) are shown (compare text). Purple: Na; gray: Sn; yellow: S; red: O.

Na–O bonds are similar to those of **I**, the average Na–S bond is significantly longer but is in agreement with literature data.[2,5,15,20] The $Na1O_3S_3$ octahedron and the $Na2O_2S_3$ trigonal bipyramid (Figure 2, bottom and Figure S8) share common edges to form a $(Na1Na2)O_3S_6$ secondary building unit, which are joined to generate a 3D network structure (Figure 2, bottom). O–H···S hydrogen bonding interactions are observed involving only the terminal S atoms of the anion.

The Raman spectra recorded in situ during 26 h show the decrease of intensity of the characteristic band of $[SnS_4]^{4-}$ (353 cm^{-1}, band **6** in Figure 3), completely vanishing and the simultaneous appearance of new bands assigned to $[Sn_2S_6]^{4-}$ (bands **1**-**5** in Figure 3). For a conclusive assignment of the bands DFT calculations were performed and the results are compared to the experimental vibrational frequencies in Table 1. Interestingly, calculation of the free $[SnS_4]^{4-}$ anion led to the breathing vibration (A_1) at 267 cm^{-1} at significantly lower frequency than in the experiment (353 cm^{-1}, band **6** in Figure 3). It seems logical that the $[SnS_4]^{4-}$ anion should be strongly affected by secondary interactions and therefore in a following calculation two coordinating Na^+ and the eight most strongly coordinating H_2O molecules were considered. The symmetry reduction led to two different stretching vibrations, one Sn–S stretch with contact to Na^+ and one without, yielding 338 cm^{-1} ($SnS_2(Na_2)$) and 356 cm^{-1} (SnS_2) fitting well to the

Table 1. Experimental vibrational frequencies (cm^{-1}) of $[SnS_4]^{4-}$ and $[Sn_2S_6]^{4-}$ in **I** and **II** and theoretical values for $\{Na_2[SnS_4](H_2O)_8\}^{2-}$ and $\{Na_2[Sn_2S_6]\}^{2-}$.

Experiment, Raman (Start)	Experiment, Raman (End)	Simulation[a]	Compound	Mode[b]' (Assignment in Figure 3)
	60/75	68	$Na_4Sn_2S_6$	A_g
	93	93	$Na_4Sn_2S_6$	A_g
			NaOH	Lattice[c]
	104	113/117	$Na_4Sn_2S_6$	A_g
	123 (m)	149	$Na_4Sn_2S_6$	$A_g(Sn_2S_2)$ (**5**)
	135 (w)		–	–
	214 (w)		NaOH	Lattice[c]
	247 (m)		$Na_4Sn_2S_6$	Lattice
	289 (m)	282	$Na_4Sn_2S_6$	$A_g(Sn_2S_2)$ (**4**)
			NaOH	Lattice[c]
	347 (vs)	344	$Na_4Sn_2S_6$	$A_g(Sn_2S_2)$ (**3**)
353 (s)		338/356	Na_4SnS_4	$\nu(SnS_2)$/ $\nu(SnS(Na)_2)$ (**6**)
	364 (s)	372	$Na_4Sn_2S_6$	A_g(Sn–S) (**2**)
	386 (s)	384	$Na_4Sn_2S_6$	A_g(Sn–S(Na)) (**1**)

Complete data in Table S6. [a] single points on SC-XRD coordinates with subsequent vibrational analysis. Only vibrations of the anions listed: $[Sn_2S_6]^{4-}$ of a $\{Na_2[Sn_2S_6]\}^{2-}$ unit for $Na_2Sn_2S_6$ and the only observable vibration of $[SnS_4]^{4-}$ inside $\{Na_2[SnS_4](H_2O)_8\}^{2-}$ for Na_4SnS_4; [b] 9 A_g (Ra) modes are listed for $[Sn_2S_6]^{4-}$ [c] Ref. [29].

Research Article
doi.org/10.1002/chem.202202318
Chemistry Europe
European Chemical Societies Publishing

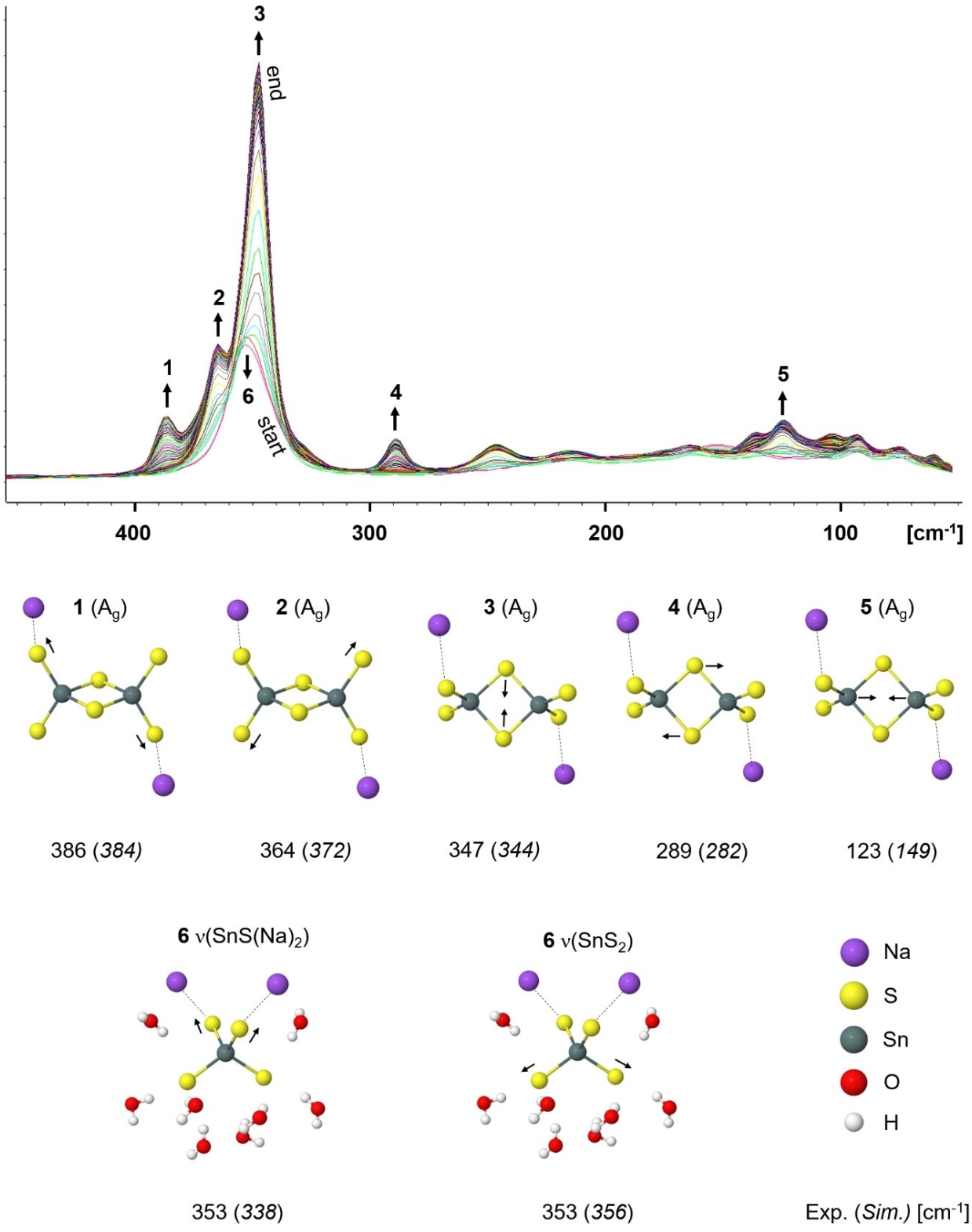

Figure 3. Time-dependent lower frequency Raman spectra of **I** (2 spectra/h · 26 h = 52 spectra) (top), showing the transformation into **II**. The strongest six bands are assigned according to results of the calculations (single points and vibrational analysis on SC-XRD coordinates including coordinating Na^+ ions and the eight strongest coordinating water molecules for $[SnS_4]^{4-}$). The A_g modes for $[Sn_2S_6]^{4-}$ with two coordinating Na^+ ions and the vibrations obtained for $[SnS_4]^{4-}$ with next nearest H_2O molecules and Na^+ ions (bottom).

experimental values (353 cm^{-1}, FWHM = 20 cm^{-1}). Obviously, secondary interactions affect the frequencies of the vibrations.

For the D_{2h} symmetric $[Sn_2S_6]^{4-}$ anion the vibrational analysis yields Equation (2):

$$\Gamma_{vib}^{D2h} = 4\ A_g\ (Ra) + 2\ B_{1g}\ (Ra) + 2\ B_{2g}\ (Ra) + 1\ B_{3g}\ (Ra) + 1\ A_u\ (inactive) + 3\ B_{1u}\ (IR) + 2\ B_{2u}\ (IR) + 3\ B_{3u}\ (IR) \quad (2)$$

Calculation of vibrations of the free $[Sn_2S_6]^{4-}$ anion led to a spectrum with only two vibrations above 300 cm^{-1} in contrast to the three visible bands between 320 and 400 cm^{-1} in the experimental spectrum increasing in intensity during the conversion process (bands **1**, **2**, and **3** in Figure 3). Like for $[SnS_4]^{4-}$, to account for the effect of a coordinating environment the two nearest Na^+ ions were included in the calculations (Figure 3) generating a $\{Na_2[Sn_2S_6]\}^{2-}$ moiety and the rule of mutual exclusion can be applied for the obtained vibrations (g: Raman active, u: IR active). For the C_i symmetric $[Sn_2S_6]^{4-}$ the vibrational analysis results in Equation 3:

$$\Gamma_{vib}^{Ci} = 9\ A_g\ (Ra) + 9\ A_u\ (IR) \quad (3)$$

This approach yields a spectrum almost perfectly reproducing the three vibrations above 300 cm^{-1}, including two types of terminal Sn–S stretching modes (bands **1** and **2** in Figure 3) and a ring deformation vibration (band **3** in Figure 3, see also Figure S9). Interestingly, the latter represents the strongest band and was earlier assigned as unspecific Sn–S stretching vibration but no explanation for three bands located above 300 cm^{-1} was given. The coordination of Na^+ on the opposite sides leads to decoupled vibrations, both totally symmetric regarding C_i, with different energies. This is in contrast to the A_g vibrations of the free anion, which is also totally symmetric but has the local symmetry D_{2h}. Accordingly, the lower change of polarizability in case of the $A_g(C_i)$ vibrations then correlates with the lower intensity of the observed Sn–S bands compared to the strong band of the Sn_2S_2 deformation vibration at 347 cm^{-1}. In the higher energy region of the Raman spectra (3500-500 cm^{-1}) the loss of H_2O during the conversion into **II** can be seen (Figure S11 and Table S6). Additionally, small amounts of Na_2CO_3, most likely originating from reaction of NaOH (see Equation (1)) and CO_2, was observed.

The H_2O loss during the transformation was monitored by in situ IR spectroscopy. Indeed, during ≈17 h the bands of water ($\nu(H_2O)$ at 3600–2900 cm^{-1} and $\delta(H_2O)$ at 1700-1500 cm^{-1}) vanished (Figure 4, Table S6). Additionally, a progressive absorption at 3520 cm^{-1} may be explained by NaOH formation during condensation of two $[SnS_4]^{4-}$ anions, which is accompanied by evolution of H_2S evidenced by the characteristic smell. The continuous decrease of absorption band intensity for H_2O can be explained by the experimental setup, where the IR chamber is continuously purged with dry N_2, and the reduced H_2O content in **II**. is done see above

Sulfidic compounds such as Na_3PS_4,[30,31] $Na_{3-x}PS_{4-x}Cl_x$,[32] Na_3SbS_4,[33,34] $Na_{11}Sn_2PS_{12}$,[35] $Na_{4-x}Sn_{1-x}Sb_xS_4$,[36] and $Na_3SbS_{4-x}Se_x$[37] were identified as good Na^+ ion conductors. Therefore, the total ionic conductivities σ_i of **I** and **II** were determined from electrochemical impedance spectroscopy (EIS) over the temperature range $T = -20$ to $+25$ °C. Even though EIS does not discriminate between H^+ and Na^+ ion motion properties, we

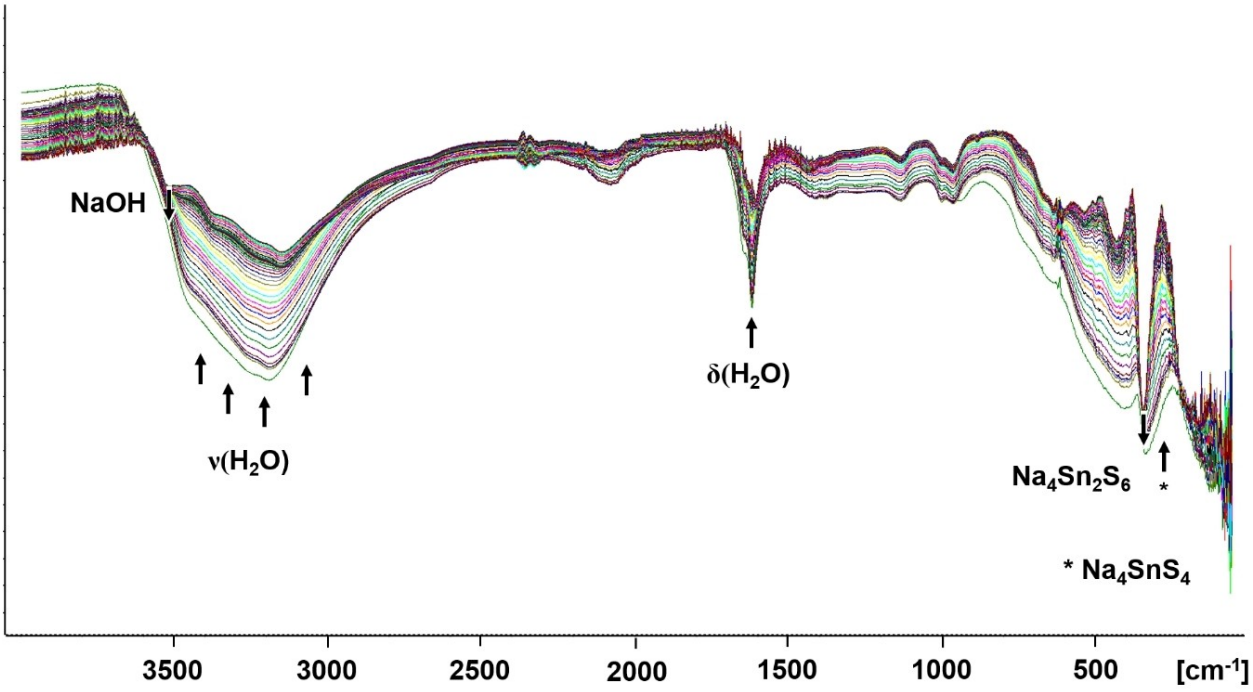

Figure 4. Time dependent IR spectra of **I** (6 spectra/h · 16.7 h = 100 spectra), showing the transformation into **II**, the loss of H_2O and NaOH formation.

expect the Na^+ ions as the dominant charge carriers (compare AIMD simulations). A representative Nyquist plot ($T = 10\,°C$) and the equivalent circuit, consisting of one constant phase element (CPE) in parallel with a resistor (R), are shown in Figure 5 (left).[31,38] This unit is connected in series to another CPE to contribute for the blocking electrode behavior. σ_i and capacitances C_i obtained at different temperatures (Figure S12 and S13) are shown in Table 2. Both samples exhibit comparable values, for example, σ_i(**I**) = 4.8 μS cm^{-1} and σ_i(**II**) = 3.9 μS cm^{-1} at $T = +10\,°C$. In the small temperature range, σ_i(**I**) and σ_i(**II**) cover several orders of magnitude (Table 2). C_i(**I**) and C_i(**II**) are similar between −20 and 25 °C (Table 2) and can be correlated to averaged bulk and grain boundary transport properties ($C_{bulk} \approx 1\times10^{-12}$ F and $C_{grain\ boundary} \approx 4\times10^{-9}$ F).[39] σ_i(**I**) and σ_i(**II**) are lower than values reported for solid-state Na^+ ion electrolytes, but reasonably high compared to that of $Na_3SbS_4 \cdot 9H_2O$ (σ_i = 0.5 μS cm^{-1} at RT).[33] Using the temperature-dependent data, the activation energies for ionic conduction E_a (Eq. (4)) were calculated using Arrhenius plots (Figure 5, right) according to Equation (4):

$$\sigma_i T = A \times \exp(-E_a/k_B T) \quad (4)$$

A = pre-exponential factor, σ_i = ionic conductivity, k_B = Boltzmann constant, T = absolute temperature.

An important observation is that σ_i(**II**) follows the Arrhenius law over the entire temperature range, whereas a deviation from the linear behavior is observed for σ_i(**I**) at $T > 10\,°C$ (Figure 5, right). This is caused by transformation of **I** into **II** during the measurement, thus a mixture of both compounds was investigated (Figure S14). Therefore, E_a(**I**) was calculated in the range from −20 to +10 °C, while E_a(**II**) was obtained for the whole temperature range (Figure S15). Comparable values of E_a(**I**) = 0.91 eV and E_a(**II**) = 0.88 eV are determined, demonstrating similar ionic conduction properties. Like for σ_i, the values for E_a are larger than for, for example, Na_3SbS_4 (0.22-0.25 eV)[33,34], $Na_{11}Sn_2PS_{12}$ (0.39 eV),[35] or $Na_3SbS_{3.75}Se_{0.25}$ (0.23 eV).[37]

Table 2. Selected ionic conductivities σ_i and capacitances C_i at various temperatures for **I** and **II**.

T [°C]	σ_i(**I**) [S cm^{-1}]	C_i(**I**) [nF]	σ_i(**II**) [S cm^{-1}]	C_i(**II**) [nF]
−20	6.5×10^{-8}	0.08	4.7×10^{-8}	0.06
−10	3.6×10^{-7}	0.08	2.6×10^{-7}	0.06
0	1.5×10^{-6}	0.08	1.1×10^{-6}	0.06
+10	4.8×10^{-6}[a]	0.08	3.9×10^{-6}	0.06
+20	1.0×10^{-5}[a]	0.09	1.1×10^{-5}	0.05
+25	9.9×10^{-6}[a]	0.07	1.7×10^{-5}	0.05

[a] σ_i deviates from linear Arrhenius behaviour, see Figure 5 (right).

In order to understand the contribution of Na^+ ion transport properties to the total σ_i, we analyzed the static energy landscape for mobile Na^+ ions by the bond valence site energy method (BVSE),[40,41] which provides a quick approximate overview on the topology of the migration pathways as well as relevant migration barriers from representative local structure models. The Na^+ ion transport in both local structure models of **I** (involving either O5, O6 and O7 or O5′, O6′ and O7′) preferentially follows a robust 2D path perpendicular to [010] (Figure 6) that involves the octahedrally coordinated Na2 and Na3 sites with $E_a \approx 0.82$–0.87 eV (depending on the local structure model), while some local structure models suggest an 1D path with a slightly lower migration barrier along [001] for the same Na^+ ions. With a somewhat higher energy barrier of about 1.1 eV the accessible pathways are expanded to a 3D network. These should be taken rather as upper limits as such static models do not factor in the relaxation of H_2O molecules in response to Na^+ hops, which depending on temperature may become significant in this compound.

DFT relaxations were used to confirm the structure models. When not imposing any symmetry restrictions the relaxation of a local structure model led to a model that was compatible

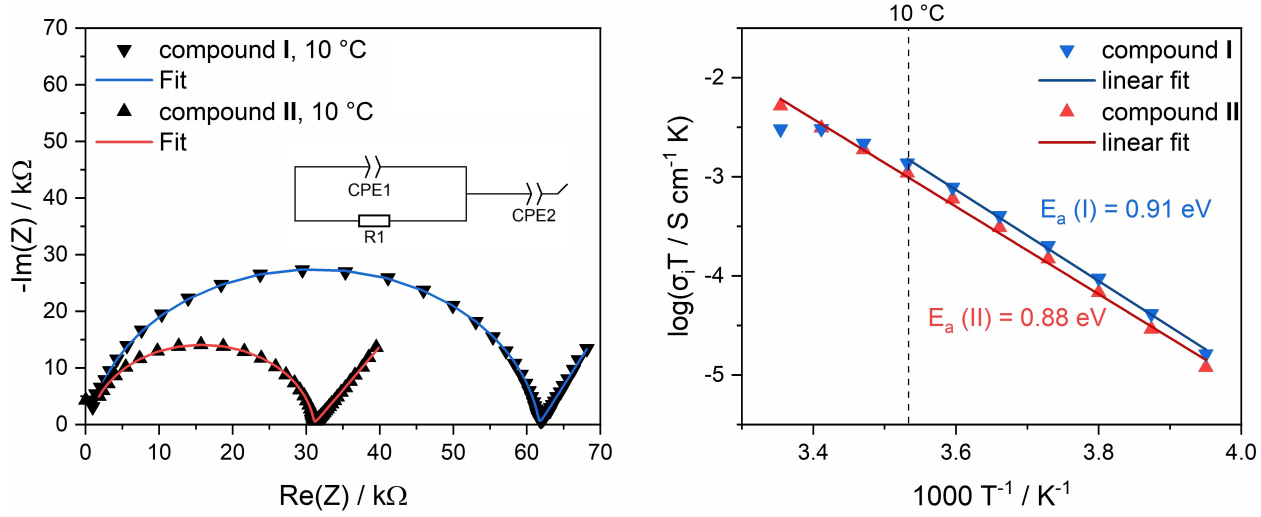

Figure 5. Nyquist impedance plots of **I** and **II** at +10 °C together with the equivalent circuit for fitting the spectra (left). Arrhenius plots of the ionic conductivity of **I** and **II** (right). For the data of **I** see explanation in the text.

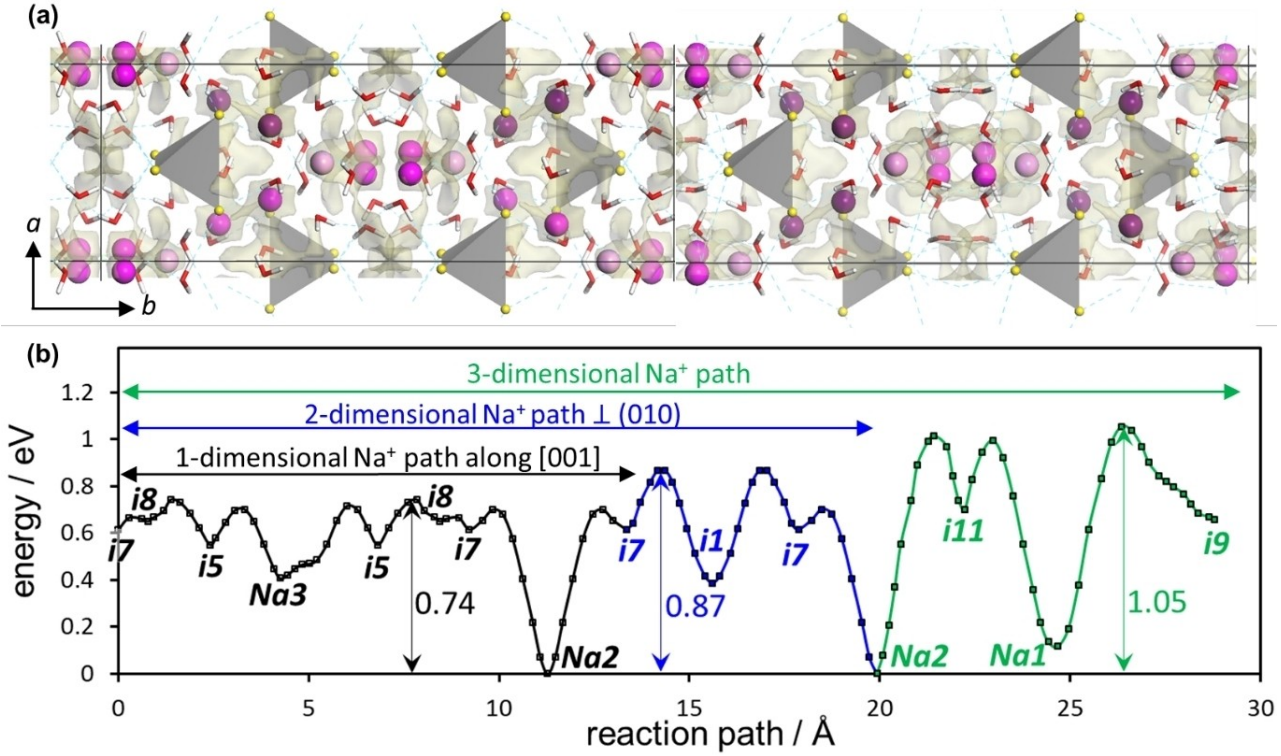

Figure 6. a) Isosurfaces of constant bond valence site energy for mobile Na^+ superimposed on a local structure model of **I** corresponding to Figure 2. Colors as in Figure 2 (Na1: dark violet sphere; Na2: light pink sphere; Na3: magenta sphere. b) Energy landscape for mobile Na^+ based on the local structure model containing O5′, O6′, O7′. Labels i# refer to interstitial sites ranked by increasing site energy.

with SG *Cc* within narrow tolerances. Non-hydrogen atom positions except the partially occupied Na3 site were also compatible with the finally chosen higher SG *C*2/*c*, supporting the plausibility of the observed structure model.

An analogous BVSE landscape for Na^+ migration in **II** yields the lowest energy percolating Na^+ paths as separate 1D paths along the *a* or *b* direction with $E_a = 0.50$ eV involving both types of Na^+ ions that are connected to form a 3D pathway network with $E_a = 0.72$ eV (Figure 7). Compared to the disorder in **I**, the diffusion in **II** is hampered by the lack of accessible sites, as all Na sites are fully occupied and the relatively high energy, interstitial sites are too close to be occupied simultaneously.

AIMD simulations of the relaxed structure model for **I** have been conducted at $T = 1200$, 800, 600 and 500 K to gain deeper insight into both the initial steps of the reaction mechanism into **II** and into the Na^+ conductivity. Due to the high computational effort, the period over which reactions can be monitored in such a 204 atom structure model is limited. Over 30 ps (steps: 1 fs) there was no bond breaking observed. This changed drastically when a water molecule dissociation was manually introduced (by converting two water molecules at a distance of 11.5 Å into OH^- and H_3O^+ groups, followed by a geometry relaxation. Independent of the temperature of the simulation the extra proton was transferred within less than 1 ps to one of the adjacent $[SnS_4]^{4-}$ groups creating $[SnS_3HS]^{3-}$ groups, while the proton vacancy at the OH^- anion became comparably mobile to the Na^+ ion through a Grotthuss type

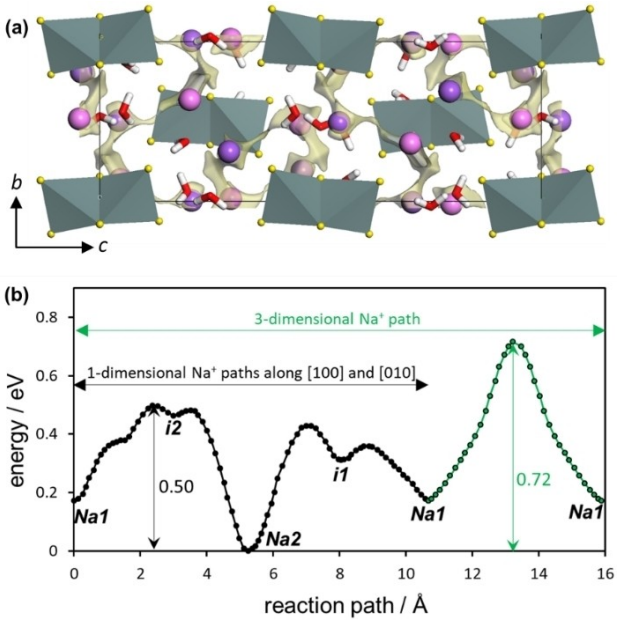

Figure 7. a) Isosurfaces of constant bond valence site energy for mobile Na^+ superimposed on the structure model of **II**. Colors as in Figure 2 (Na1: light pink sphere; Na2: dark violet sphere), b) Energy landscape for mobile Na^+ in **II**. Labels i# refer to interstitial sites ranked by increasing site energy.

mechanism. However, due to the low concentration of dissociated H_2O molecules in **I** the Na^+ ions will still remain the

dominant charge carriers. For the NVT AIMD simulations at 800 and 1200 K, the lengthening of the Sn–SH bond also led to a temporary breaking of the $[SnS_3HS]^{3-}$ group into $[SnS_3]^{2-}$ and HS^- suggesting a likely reaction path for the condensation to $[Sn_2S_6]^{4-}$.

Analysis of the mean square displacements of the Na^+ ions in **I** demonstrates a somewhat higher local mobility of Na2 and Na3 than of Na1. In line with predictions from the BVSE model (Figure 6), the Na^+ mobility remains essentially restricted to the x-z plane and only for $T = 1200$ K a significant contribution from transport along the y direction is noted. In the Arrhenius plot (Figure 8), the mean square Na displacement is converted to a Na^+ ionic conductivity applying the Nernst-Einstein equation, i.e. assuming uncorrelated hops. At T = 500–1200 K, where a statistically significant ionic motion was observed, E_a for the ion migration appears somewhat smaller and temperature dependent (see curvature of Arrhenius plot). Linear extrapolation of the AIMD results over T = 500–1200 K down to 300 K suggest ion diffusion coefficients of $D(Na) = 7 \times 10^{-12}\ m^2 s^{-1}$ and $D(H) = 6 \times 10^{-12}\ m^2 s^{-1}$ at 300 K. At least at elevated temperatures the ionic transport is more accurately described by a Vogel-Fulcher-Tammann (VFT) type temperature dependence. AIMD data and σ_i from EIS experiments can effectively be fitted by a common VFT curve (Figure 8), where the temperature dependence of E_a is characterized by a characteristic temperature T_0 of 145 K. This VFT fit corresponds to a Na^+ diffusion coefficient of $D(Na) = 6 \times 10^{-14}\ m^2 s^{-1}$ at 300 K. The VFT-type temperature dependence may be taken as a sign that ionic conductivity may show a temperature dependent transition between a liquid-like and a solid-like ion transport.

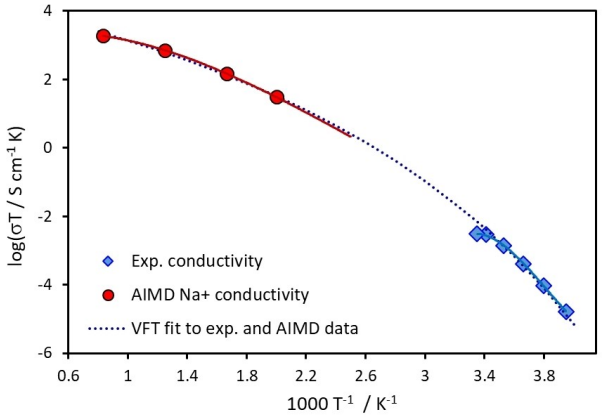

Figure 8. Arrhenius plots of experimental and simulation results for the ionic conductivity of **I**. Low temperature results from EIS (blue diamonds, same data as in Figure 5) and high temperature Na^+ ionic conductivities from AIMD simulations (red circles) can be interpreted as falling onto a common VFT-type temperature dependence (dotted line). Solid lines refer to polynomial regressions of the respective data category.

Magic-angle spinning (MAS) NMR spectroscopy was performed to gain deeper insight into the atomic environments of ^1H, ^{23}Na, and ^{119}Sn in **I** and **II** (Figure 9, full spectra see Figure S16–S18). For **I**, three signals at $\delta = 61.6$ (strong), 68.2 (medium) and 72.8 ppm (weak) are observed for ^{119}Sn. Only one unique Sn is present in this structure and the observation of more than one NMR signal indicates structural disorder, i.e. different atomic arrangements around this unique site. Moreover, the ^{119}Sn MAS NMR experiment lasted ~17 h and some **I** is already at the beginning of the phase transformation involving the S^{2-} protonation. This non-stationary situation leads to different NMR signals resulting from the $[SnS_4]^{4-}$ unit in **I** but also in intermediates with different Sn···S···H interactions. δ is in the same range as those reported for Na_4SnS_4 and K_4SnS_4 (δ = 67.6 and 74 ppm, respectively).[11,42,43] The ^1H spectrum contains only one narrow intense signal ($\delta = 5.0$ ppm), explainable by a high proton mobility. Similarly, in the ^{23}Na spectrum only one

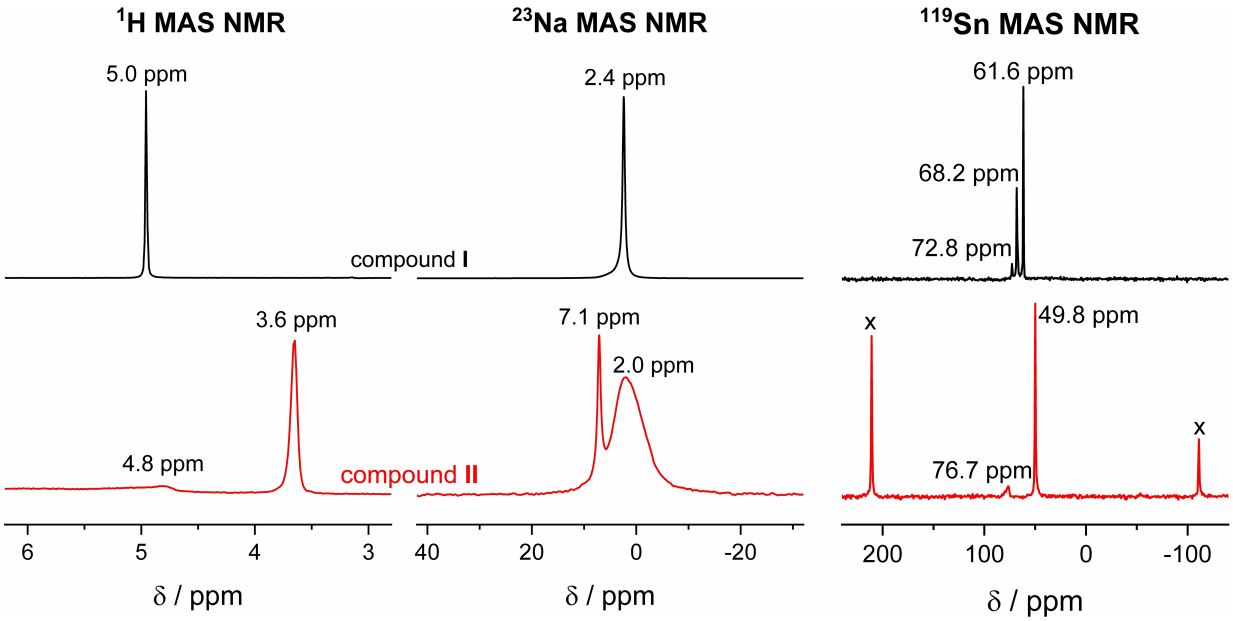

Figure 9. MAS ^1H, ^{23}Na, and ^{119}Sn MAS NMR spectra for **I** (black) and **II** (red); crosses indicate rotational sidebands.

narrow signal ($\delta = 5.0$ ppm) occurs indicating fast Na^+ ion dynamics.

In the ^{119}Sn MAS NMR spectrum of **II** (Figure 9, right, bottom) one narrow intense signal of $[Sn_2S_6]^{4-}$ is observed at $\delta = 49.8$ ppm in agreement with $\delta = 50$ ppm of $K_4Sn_2S_6$.[42] A comparable change of the ^{119}Sn NMR shift was reported for $[SnS_4]^{4-}$ and $[Sn_2S_6]^{4-}$ in solution.[11,42] A second weak signal at 76.7 ppm results from minor impurities which were not detected by XRPD. Similarly, the ^1H MAS NMR spectrum of **II** (Figure 9, left, bottom) contains one strong and one weak signal at $\delta = 3.6$ and 4.8 ppm. While in the ^{23}Na MAS NMR of **I** only one signal was observed, the spectrum of **II** (Figure 9, middle, bottom) includes two intensive signals at $\delta = 2.0$ (broad) and 7.1 ppm (narrow). Therefore, the temporal averaging of local environments is less effective, i.e. the motion of Na^+ ions seems to be slower, in agreement with the two different Na^+ environments (see above).

The phase transformation of **I** into **II** was investigated by in situ (static) solid-state ^1H NMR (Figure 10 and Figure S19). In contrast to the MAS NMR experiments this static measurement was performed in an open tube to prevent the influence of gas pressure due to H_2S and H_2O formation, hence without sample rotation. This yields broader line shapes, making a reliable differentiation of signals from **I** and **II** impossible. Therefore, the total integral intensity resulting from superposition of both compounds is plotted in Figure 10. For comparison, solid-state ^1H NMR was performed for possible other reaction products like $NaOH \cdot xH_2O$ and $NaHCO_3$ (Figure S19) with (30 kHz) and without sample rotation. Using sample rotation, one broad signal at about −3.8 ppm could be observed for $NaOH \cdot xH_2O$ and one broad peak at +13.9 ppm for $NaHCO_3$. A theoretical intensity loss of ~82% is calculated for the complete phase transformation in Equation (1) taking only **I** and **II** into account disregarding all other reaction products. Over 100 h of the in situ experiment, a linear loss in integral intensity by ~31% is observed (Figure 10, right), suggesting a reaction turnover of ~38% over this period (0.38%/h).

Conclusion

We observed an unusual structural transformation of the crystal water-rich compound $Na_4SnS_4 \cdot 14H_2O$ into the crystal water deficient sample $Na_4Sn_2S_6 \cdot 5H_2O$ at RT, which was monitored with time-resolved XRPD experiments, in situ IR, in situ Raman and in situ ^1H NMR spectroscopy. This transformation is exciting with respect to several aspects: the reaction requires a complex sequence of chemical reactions including O–H bond breakage accompanied by proton transfer to terminal S atoms of $[SnS_4]^{4-}$ units, formation of NaOH, movement of adjacent SnS_3SH^{3-} units over several Å, condensation to generate $[Sn_2S_6]^{4-}$, release of H_2S, rearrangement of the Na^+ ions including bond formation. All these processes occur in the solid state without significant changes of the crystal integrity. The reaction is slow and can be suppressed by cooling $Na_4SnS_4 \cdot 14H_2O$, indicating that the transformation is a thermally activated process. AIMD calculations support these experimental findings. EIS investigations demonstrate that **I** and **II** are moderate ionic conductors, which is underlined by data obtained from BVSE calculations, and the ionic mobility increases by three orders of magnitude between −20 to +25 °C.

Experimental Section

Synthesis of $Na_4SnS_4 \cdot 14H_2O$ (I): 1.80 g (7.50 mmol) $Na_2S \cdot 9H_2O$ were dissolved in 5 mL H_2O. 0.655 g (1.87 mmol) $SnCl_4 \cdot 5H_2O$ also dissolved in H_2O (3 mL) were added dropwise to the $Na_2S \cdot 9H_2O$ solution.[15] The mixture was stirred for 30 min at RT until the generated yellow precipitate was dissolved and a blue-green solution is formed. To this solution, 4 mL cold (3 °C) pure acetone

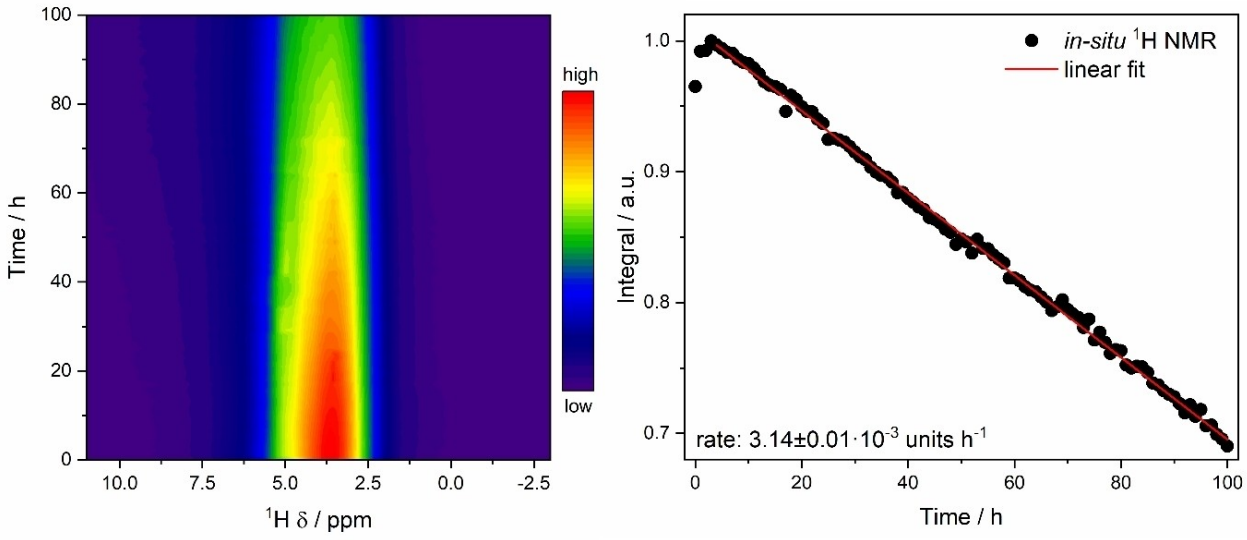

Figure 10. Time-dependent in situ solid-state (static) ^1H NMR experiment of the phase transformation of **I** (left). Change of the ^1H NMR integral intensity vs. time during the static in situ measurement (right). For further details see the plain text.

were added and stored at this temperature for 10 min. The colorless crystals were filtrated with a yield of ≈68% based on Sn.

Synthesis of $Na_4Sn_2S_6 \cdot 5H_2O$ (II): 0.750 g (1.27 mmol) $Na_4SnS_4 \cdot 14H_2O$ was dispersed in 4 mL MeOH and heated for 20 min at 90 °C. The white solid of $Na_4Sn_2S_6 \cdot 5H_2O$ was filtrated, washed with MeOH and stored in air at room temperature (yield ≈40% based on Sn). The XRPD pattern shows only reflections of compound **II** (Figure S7).

Structure Determination: Data for compound **I** were collected using a XtaLAB Synergy, Dualflex, HyPix diffractometer with Mo-K_α radiation ($\lambda = 0.71073$ Å) at 79.9(8) K. Data reduction, scaling and absorption corrections were performed using CrysAlisPro (Rigaku, V1.171.41.93a, 2020). The final completeness is 99.90% out to 30.078° in θ. A multi-scan absorption correction was performed using CrysAlisPro 1.171.41.93a (Rigaku Oxford Diffraction, 2020) using spherical harmonics, implemented in SCALE3 ABSPACK scaling algorithm. The structure was solved and the space group *C*2/*c* determined by the ShelXT[44,45] structure solution program using the Intrinsic Phasing solution method and by using Olex2[46] as the graphical interface. The model was refined with version 2016/6 of ShelXL.[44,45] All non-hydrogen atoms were refined anisotropically. The O–H H atoms were located in difference maps, their bond lengths were set to ideal values and finally they were refined isotropically with $U_{iso}(H) = 1.5\ U_{eq}(O)$ using the riding model. Selected crystal data and refinement results are summarized in Table S1 and details of the structure determinations are given in the corresponding text in the Supporting Information.

The XRPD pattern of **II** could be indexed with a tetragonal unit cell with extinction conditions suitable for the space group $P4_12_12$ using TOPAS Academic.[47] Using these parameters and an estimated composition based on EDX spectroscopy, the position of the heavy Sn, S and Na atoms could be determined using direct methods as implemented in Expo 2009.[48] This initial structure model was subsequently refined by Rietveld methods using a Thompson-Cox-Hastings profile function and a 12th order polynomial background function. Residual electron density was identified by Fourier synthesis and attributed to oxygen atoms representing water molecules coordinated to the sodium atoms. The positions of all atoms were freely refined without any restraints, and the displacement parameters were refined element specifically. The final plot is shown in Figure S7 and some figures of merit are summarized in Table S4. Our structural data derived from the XRPD pattern match very well with those reported in the Supporting Information of Ref. [21].

Deposition Numbers 2142577 (**I** at 100 K), 2142575 (**I** at 140 K), 2142574 (**I** at 180 K), 2142573 (**I** at 220 K), 2142576 (**I** at 260 K) and 1984037 (**II**) contain the supplementary crystallographic data for this paper. These data are provided free of charge by the joint Cambridge Crystallographic Data Centre and Fachinformationszentrum Karlsruhe Access Structures service.

Computational Details: First-principles DFT calculations for the molecular dynamics simulations were carried out under the generalized gradient approximation[49] with the Vienna ab initio Simulation Package[50,51] (for energy minimizations) and with CASTEP[52] for the dynamic simulations. Calculations of the vibrational spectra were carried out by using the TURBOMOLE program package.[53] Structure optimizations were performed at the PBE05/def2-TZVPP[54–56] level of theory and RI approximation[57–59] to speed up the calculations. To prove that the optimized structure is a minimum on the potential energy surface and for the vibrational frequencies the AOFORCE module was used,[60] which is included in the TURBOMOLE program package.

AIMD simulations were conducted for a conventional unit cell $Na_{16}Sn_4S_{16}H_{112}O_{56}$ containing 204 atoms using a 380 eV plane-wave energy cutoff with time steps of 1 fs in the canonical (NVT) ensemble for four temperatures, 1200 K, 800 K, 600 K and 500 K over 10–30 ps. Additional trials with longer time steps up to 2 fs to facilitate longer simulation periods led to an unphysical behavior of the O–H bonds and thus had to be discarded. For each time step total energy/atom was converged to 2×10^{-6} eV and eigen energy was converged to 10^{-6} eV. As preliminary simulations of the ordered structure at 800 K did not result in any chemical reaction over the simulation period, AIMD simulations discussed in this work refer to a 204 atoms local structure model comprising a conventional unit cell where the chemical reaction was accelerated by dissociating one water molecule (containing an O(7) atom) into an OH group and a symmetry copy of this water molecule at a distance of 11.5 Å into an H_3O group, followed by a geometry relaxation.

X-Ray Powder Diffraction: The XRPD patterns were measured with a STOE Stadi-P diffractometer equipped with a MYTHEN 1 K detector (DECTRIS) in transmission geometry using monochromatized Cu-$K_{\alpha 1}$ radiation ($\lambda = 1.540598$ Å).

Infrared Spectroscopy: IR spectra were recorded at RT on a Bruker Vertex70 FTIR spectrometer using a broadband spectral range extension VERTEX FM for full, mid, and far IR in the range of 6.000-80 cm^{-1}.

Raman Spectroscopy: Raman spectra were recorded at RT on a Bruker RAM II FT-Raman spectrometer using a liquid nitrogen cooled, highly sensitive Ge detector, 1064 nm radiation and 4 cm^{-1} resolution.

Electrochemical Impedance Spectroscopy: EIS was performed using a VSP Essential (BioLogic) and an impedance test cell for solids ASC–A (Sphere™) exhibiting stainless steel pistons as blocking electrodes. The solid compounds were pressed into pellets at RT ($p \approx 120$ MPa, diameter $d = 8.0$ mm, thickness h(**I**) = 1.49 mm, h(**II**) = 0.59 mm). The cell was cooled to −20 °C in a climate chamber MK056 (Binder) and three impedance measurements were recorded with an amplitude of 100 mV in a frequency range from 1 MHz to 1 Hz after a resting time of 3.5 h at various temperatures between −20 and +25 °C with T steps of +5 °C. The total ionic conductivity was calculated from the impedance spectra applying fits according to the equivalent circuit shown in Figure 5 (left) using EC-Lab® V11.33.

Solid-State MAS NMR Spectroscopy: ^{1}H, ^{23}Na, and ^{119}Sn MAS NMR was performed at a magnetic field of 11.7 T, corresponding to resonance frequencies of 500.2 MHz, 132.3 MHz, and 186.5 MHz, respectively. Powder samples were packed into 2.5 mm rotors in argon atmosphere and the spinning speed was 30 kHz. Spectra were acquired with a single-pulse sequence for ^{1}H/^{119}Sn and with a Hahn-echo sequence for ^{23}Na. The $\pi/2$ pulse length was 4.2 µs for ^{1}H, 2.65 µs for ^{23}Na, and 1.2 µs for ^{119}Sn. The recycle delay was 15 s for ^{1}H and 30 s for ^{23}Na/^{119}Sn. Chemical shifts were referenced to tetramethylsilane for ^{1}H (0 ppm), an aqueous 1 M NaCl solution for ^{23}Na (0 ppm), and well crystalline SnO_2 for ^{119}Sn (−604.3 ppm).[61]

Acknowledgements

Financial support to W. B. by the State of Schleswig-Holstein and to S. A. by the Singapore Ministry of Education in the frame of the AcRF grant R-284-000-250-114 is gratefully acknowledged. Open Access funding enabled and organized by Projekt DEAL.

Conflict of Interest

The authors declare no conflict of interest.

Data Availability Statement

The data that support the findings of this study are available from the corresponding author upon reasonable request.

Keywords: AIMD simulations · Raman spectroscopy · Infrared spectroscopy · Ionic conductivity · Magic angle spinning NMR · Epitaxy

[1] G. A. Marking, M. Evain, V. Petricek, M. G. Kanatzidis, *J. Solid State Chem.* **1998**, *141*, 17–28.
[2] M. S. Devi, K. Vidyasagar, *J. Chem. Soc. Dalton Trans.* **2002**, 2092–2096.
[3] C. L. Teske, *Z. Anorg. Allg. Chem.* **1978**, *445*, 193–201.
[4] C. L. Teske, *Z. Anorg. Allg. Chem.* **1980**, *460*, 163–168.
[5] A. Kumari, K. Vidyasagar, *J. Solid State Chem.* **2007**, *180*, 2013–2019.
[6] B. Seidlhofer, N. Pienack, W. Bensch, *Z. Naturforsch.* **2010**, *65b*, 937–975.
[7] N. Pienack, W. Bensch, *Z. Anorg. Allg. Chem.* **2006**, *632*, 1733–1736.
[8] N. Pienack, K. Möller, C. Näther, W. Bensch, *Solid State Sci.* **2007**, *9*, 1110–1114.
[9] N. Pienack, C. Näther, W. Bensch, *Solid State Sci.* **2007**, *9*, 100–107.
[10] A. Benkada, M. Poschmann, C. Näther, W. Bensch, *Z. Anorg. Allg. Chem.* **2019**, *645*, 433–439.
[11] A. Benkada, H. Reinsch, M. Poschmann, J. Krahmer, N. Pienack, W. Bensch, *Inorg. Chem.* **2019**, *58*, 2354–2362.
[12] M. Behrens, M.-E. Ordolff, C. Näther, W. Bensch, K.-D. Becker, C. Guillot-Deudon, A. Lafond, J. A. Cody, *J. A. Inorg. Chem.* **2010**, *49*, 8305–8309.
[13] Z. H. Fard, C. Müller, T. Harmening, R. Pöttgen, S. Dehnen, *Angew. Chem. Int. Ed.* **2009**, *48*, 4441–4444; *Angew. Chem.* **2009**, *121*, 4507–4511.
[14] H. P. Nayek, W. Massa, S. Dehnen, *Inorg. Chem.* **2008**, *47 (20)*, 9146–9148.
[15] W. Schiwy, S. Pohl, B. Krebs, *Z. Anorg. Allg. Chem.* **1973**, *402*, 77–86.
[16] F. Hartmann, A. Benkada, S. Indris, M. Poschmann, H. Lühmann, P. Duchstein, D. Zahn, W. Bensch, *Angew. Chem. Int. Ed.* **2022**, *61*, e202202182; *Angew. Chem.* **2022**, *134*, e202202182.
[17] R. D. Willett, A. Vij, J. M. Imhof, D. A. Cleary, *J. Chem. Crystallogr.* **2000**, *30*, 405–410.
[18] R. D. Shannon, *Acta Crystallogr. A* **1976**, *32*, 751–767.
[19] B. Krebs, S. Pohl, W Schiwy, *Z. Anorg. Allg. Chem.* **1972**, *393*, 241–252.
[20] H. Lühmann, C. Näther, I. Jess, W. Bensch, *Z. Anorg. Allg. Chem.* **2019**, *645*, 1165–1170.
[21] Y. K. Kang, H. Lee, T. D. Cam Ha, J. Kook Won, H. Jo, K. Min Ok, S. Ahn, B. Kang, K. Ahn, Y. Oh, M.-G. Kim, *J. Mater. Chem. A* **2020**, *8*, 3468–3480.
[22] J. Hilbert, N. Pienack, H. Lühmann, C. Näther, W. Bensch, *Z. Anorg. Allg. Chem.* **2016**, *642*, 1427–1434.
[23] D.-X. Jia, Y. Zhang, J. Dai, Q.-Y. Zhu, X.-M. Gu, *Z. Anorg. Allg. Chem.* **2004**, *630*, 313–318.
[24] D.-X. Jia, J. Dai, Q.-Y. Zhu, Y. Zhang, X.-M. Gu, *Polyhedron* **2004**, *23*, 937–942.
[25] Q. Jin, J. Chen, Y. Pan, Y. Zhang, D. Jia, *J. Coord. Chem.* **2010**, *63*, 1492–1503.
[26] N. Pienack, C. Näther, W. Bensch, *Z. Naturforsch.* **2008**, *63b*, 1243–1251.
[27] J. Zhou, X. Liu, L. An, F. Hu, W. Yan, Y. Zhang, *Inorg. Chem.* **2012**, *51*, 2283–2290.
[28] M. Behrens, S. Scherb, C. Näther, W. Bensch, *Z. Anorg. Allg. Chem.* **2003**, *629*, 1367–1373.
[29] D. Krishnamurti, *Proc. Indian Acad. Sci. A* **1959**, *50*, 223–231.
[30] A. Hayashi, K. Noi, A. Sakuda, M. Tatsumisago, *Nat. Commun.* **2012**, *3*, 856.
[31] T. Krauskopf, S. P. Culver, W. G. Zeier, *Inorg. Chem.* **2018**, *57*, 4739–4744.
[32] I.-H. Chu, C. S. Kompella, H. Nguyen, Z. Zhu, S. Hy, Z. Deng, Y. S. Meng, S. P. Ong, *Sci. Rep.* **2016**, *6*, 33733.
[33] H. Wang, Y. Chen, Z. D. Hood, G. Sahu, A. S. Pandian, J. K. Keum, K. An, C. Liang, *Angew. Chem. Int. Ed.* **2016**, *55*, 8551–8555; *Angew. Chem.* **2016**, *128*, 8693–8697.
[34] L. Zhang, D. Zhang, K. Yang, X. Yan, L. Wang, J. Mi, B. Xu, Y. Li, *Adv. Sci.* **2016**, *3*, 1600089.
[35] M. Duchardt, U. Ruschewitz, S. Adams, S. Dehnen, B. Roling, *Angew. Chem. Int. Ed.* **2018**, *57*, 1351–1355; *Angew. Chem.* **2018**, *130*, 1365–1369.
[36] J. W. Heo, A. Banerjee, K. H. Park, Y. S. Jung, S.-T. Hong, *Adv. Energy Mater.* **2018**, *8*, 1702716.
[37] H. Wan, J. P. Mwizerwa, F. Han, W. Weng, J. Yang, C. Wang, X. Yao, *Nano Energy* **2019**, *66*, 104109.
[38] S. Hori, K. Suzuki, M. Hirayama, Y. Kato, R. Kanno, *Front. Energy Res.* **2016**, *4*, 38.
[39] J. T. S. Irvine, D. C. Sinclair, A. R. West, *Adv. Mater.* **1990**, *2*, 132–138.
[40] L. L. Wong, K. C. Phuah, R. Dai, H. Chen, W. S. Chew, S. Adams, *Chem. Mater.* **2021**, *33*, 625–641.
[41] H. Chen, L. L. Wong, S. Adams, *Acta Crystallogr. B* **2019**, *75*, 18–33.
[42] L. Protesescu, M. Nachtegaal, O. Voznyy, O. Borovinskaya, A. J. Rossini, L. Emsley, C. Copéret, D. Günther, E. H. Sargent, M. V. Kovalenko, *J. Am. Chem. Soc.* **2015**, *137*, 1862–1874.
[43] C. Mundus, G. Taillades, A. Pradel, M. A. Ribes, *Solid State Nucl. Magn. Reson.* **1996**, *7*, 141–146.
[44] G. M. Sheldrick, *Acta Crystallogr. A* **2015**, *71*, 3–8.
[45] G. M. Sheldrick, *Acta Crystallogr. C* **2015**, *71*, 3–8.
[46] O. V. Dolomanov, L. J. Bourhis, R. J. Gildea, J. A. K. Howard, H. Puschmann, *J. Appl. Crystallogr.* **2009**, *42*, 339–341.
[47] A. A. Coelho, *J. Appl. Crystallogr.* **2018**, *51*, 210–218.
[48] A. Altomare, M. Camalli, C. Cuocci, C. Giacovazzo, A. Moliterni, R. Rizzi, *J. Appl. Crystallogr.* **2009**, *42*, 1197–1202.
[49] J. P. Perdew, K. Burke, M. Ernzerhof, *Phys. Rev. Lett.* **1996**, *77*, 3865–3868.
[50] G. Kresse, J. Furthmüller, *Phys. Rev. B* **1996**, *54*, 11169–11186.
[51] G. Kresse, J. Furthmüller, *Comput. Mater. Sci.* **1996**, *6*, 15–50.
[52] S. J. Clark, M. D. Segall, C. J. Pickard, P. J. Hasnip, M. J. Probert, K. Refson, M. C. Payne, *Z. Kristallogr.* **2005**, *220*, 567–570.
[53] R. Ahlrichs, M. Bär, M. Häser, H. Horn, C. Kölmel, *Chem. Phys. Lett.* **1989**, *162*, 165–169.
[54] A. Hellweg, C. Hättig, S. Höfener, W. Klopper, *Theor. Chem. Acc.* **2007**, *117*, 587–597.
[55] F. Weigend, *Phys. Chem. Chem. Phys.* **2006**, *8*, 1057–1065.
[56] F. Weigend, R. Ahlrichs, *Phys. Chem. Chem. Phys.* **2005**, *7*, 3297–3305.
[57] K. Eichkorn, O. Treutler, H. Öhm, M. Häser, R. Ahlrichs, *Chem. Phys. Lett.* **1995**, *240*, 283–290.
[58] K. Eichkorn, F. Weigend, O. Treutler, R. Ahlrichs, *Theor. Chem. Acc.* **1997**, *97*, 119–124.
[59] F. Neese, *J. Comput. Chem.* **2003**, *24*, 1740–1747.
[60] O. Treutler, R. Ahlrichs, *J. Chem. Phys.* **1995**, *102*, 346–354.
[61] N. J. Clayden, C. M. Dobson, A. Fern, *J. Chem. Soc. Dalton Trans.* **1989**, 843–847.

Manuscript received: July 25, 2022
Accepted manuscript online: October 10, 2022
Version of record online: November 16, 2022